

Intervalley scattering and localization behaviors of spin-valley coupled Dirac fermions

Hai-Zhou Lu,¹ Wang Yao,¹ Di Xiao,² and Shun-Qing Shen¹

¹*Department of Physics and Centre of Theoretical and Computational Physics,
The University of Hong Kong, Pokfulam Road, Hong Kong, China*

²*Department of Physics, Carnegie Mellon University, Pittsburgh, Pennsylvania 15213, USA*

(Dated: January 18, 2022)

We study the quantum diffusive transport of multi-valley massive Dirac cones coupled by intervalley spin-orbit scattering. We show that the intervalley spin-orbit scattering and intravalley spin-conserved scattering can be distinguished from the quantum conductivity that corrects the semiclassical Drude conductivity, due to their distinct symmetries and localization trends. In immediate practice, it allows transport measurements to estimate the intervalley scattering rate in hole-doped monolayers of group-VI transition metal dichalcogenides (e.g., molybdenum dichalcogenides and tungsten dichalcogenides), an ideal class of materials for valleytronics applications. The results can be generalized to a large class of multi-valley massive Dirac systems where time-reversal symmetry demands opposite spins in opposite valleys.

PACS numbers: 73.63.-b, 75.70.Tj, 85.75.-d

Valley index associated the degenerate energy extrema of Bloch bands in momentum space is a well defined degree of freedom for low-energy carriers which can encode information just like the spin index in spintronics. This has led to the concept of valleytronics, a new type of electronics based on manipulating the valley index of carriers [1–5]. The timescale of intervalley scattering determines how long the information represented by valley polarization can be retained. For valleytronics applications to be practical, this timescale shall be long as compared to the typical time for the control of valley dynamics. Measurement of intervalley scattering time is thus critical for identifying potential valleytronics materials.

Several extensively studied monolayer 2D crystals are promising materials to host valley-based electronics, including graphene, and graphene-like crystals such as silicene [6–10] and monolayer group-VI transition metal dichalcogenides [11–14]. In these hexagonal 2D crystals, both the conduction and valence band edges are at the two inequivalent valleys at K points (corners of first Brillouin zone), which are related by time reversal. In monolayer dichalcogenides, ground breaking theoretical and experimental progresses on dynamical control of valley are recently achieved [15–18]. Unlike graphene, monolayer dichalcogenides are described by massive Dirac fermions, and intrinsic spin-orbit coupling (SOC) gives rise to a spin splitting which must have opposite sign at the two valleys by the requirement of time reversal symmetry (see e.g. Fig. 1). This effective coupling between the spin and valley indices can have two significant consequences for valleytronics: (i) the interplay between spin and valley degrees of freedom; (ii) a unique form of intervalley scattering which must be accompanied by a simultaneous spin flip.

In this Letter, we study the quantum diffusive transport of multi-valley massive Dirac fermions with spin-valley coupling. Without loss of generality we choose the

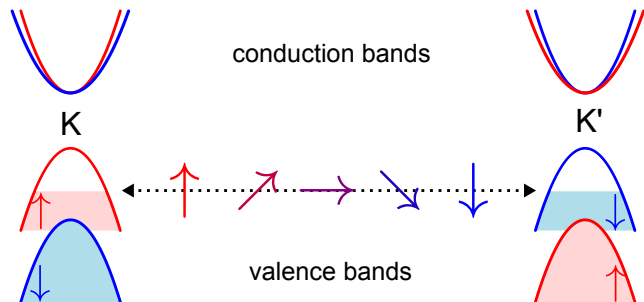


FIG. 1: Low-energy effective band structures of MX_2 monolayer in K and K' valleys. The Fermi surface (at the top edges of shadowed areas) intersects the highest two valence bands of opposite spin orientations (marked by \uparrow and \downarrow). Horizontal dotted arrows guide the intervalley spin-flip scattering assisted by spin-orbit interaction.

model of monolayer dichalcogenides MX_2 ($M = \text{Mo}, \text{W}$; $X = \text{S}, \text{Se}$) for a concrete discussion. This problem is theoretically unique from the conventional 2D electron gas systems or the massless graphene systems without spin-orbit coupling. We show that the spin-valley coupled band edge results in distinct symmetries and localization behaviors in intra- and inter-valley scattering dominant regimes. Namely, the spin-conserving intravalley scattering leads to negative quantum conductivity and positive magnetoconductivity from weak localization (WL) effect, whereas the intervalley scattering assisted by spin-orbit interaction gives rise to positive quantum conductivity and negative magnetoconductivity from weak antilocalization (WAL). The quantum conductivity and magnetoconductivity have logarithmic dependence on the ratio between intra- and inter-valley scattering rates. Such a dependence makes possible measurement of intervalley scattering rate in a vastly broad range in monolayer dichalcogenides, from three orders of magnitude below to three orders of magnitude above the intravalley scatter-

ing rate, which can be readily tested in available dichalcogenide field effect transistors [19–21]. Experimental verifications of these phenomena will reveal the nature of impurities and provide general guidance on the suppression of intervalley scattering for a longer valley life time necessary for valleytronic applications. Our approach and results can also be readily extended to spin-valley coupled Dirac fermions with much smaller masses in silicene or monolayers of germanium and tin [6].

The band edge electrons and holes in monolayer MX_2 are well described by the massive Dirac fermion model [15]:

$$H = \hbar v(\pm k_x \hat{\sigma}_x + k_y \hat{\sigma}_y) + \frac{\Delta}{2} \hat{\sigma}_z \pm \lambda \hat{s}_z \otimes \frac{\hat{1} - \hat{\sigma}_z}{2}, \quad (1)$$

where \pm stands for K and K' valleys, respectively. The Pauli matrices $\sigma_{x,y,z}$ act on the pseudospin indexing the $A \equiv d_{z^2}$ and $B \equiv (d_{x^2-y^2} \pm id_{xy})/\sqrt{2}$ orbitals while $s_z = \uparrow, \downarrow$ is the z -component of real spins. (k_x, k_y) is the wave vector measured from K (K') points. The Hamiltonian is described by three parameters: the SOC strength λ , the band gap Δ , and the effective velocity v . The resulting band structure consists of four sets of massive Dirac cones, two in K and two in K' valleys. An important feature is the large SOC splitting [15, 22] ($2\lambda \sim 0.15$ eV in molybdenum dichalcogenides and $2\lambda \sim 0.4$ eV in tungsten dichalcogenides) between the spin-up and spin-down states at the valence band top. The conduction band bottoms remain degenerate. The band dispersion is schematically shown in Fig. 1.

Because of the large spin splitting in the valence bands, in the following we focus on the localization effect in hole-doped samples. It is instructive to first consider two limiting regimes when either intra- or inter-valley scattering dominates.

(1) Intravalley scattering dominant regime. In the valence bands, when holes are confined to a single valley, the SOC acts like a strong Zeeman field, which fully polarizes the spins. Therefore, the intravalley scattering can only happen between the same spin species. At the same time, because of the large band gap ($\Delta \sim 1.6$ eV), the orbital pseudospin is almost fully-polarized and does not play a role. The frozen pseudospin can be quantitatively seen from the Berry phase [23], which for the valence bands is given by

$$\phi_v = 2\pi \frac{V + \Delta - \lambda}{2V + \Delta - \lambda} \sim 2\pi \quad (2)$$

where V measures the Fermi energy from the valence band top. Δ is much larger than λ and allowed $V \in [0, 2\lambda]$ eV in MX_2 [15]. The spin-conserved intravalley scattering that also conserves time-reversal symmetry belong to the orthogonal symmetry class [24], which gives rise to WL [25].

(2) Intervalley scattering dominant regime. The intervalley scattering in MX_2 must break spin-rotational

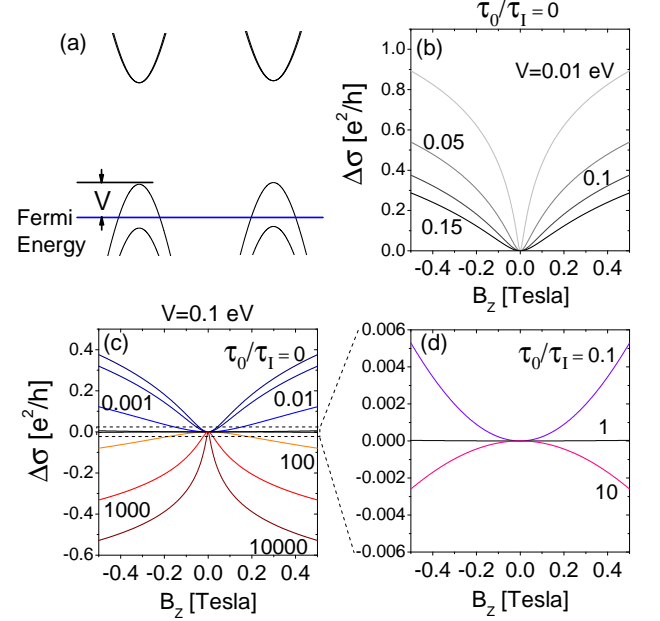


FIG. 2: (a) Sketch of band structure, where $V \in [0, 2\lambda]$ eV measures the Fermi energy from the valence band top. [(b)-(d)] Magnetoconductivity $\Delta\sigma$ under a perpendicular magnetic field B_z , and when the Fermi energy intersects the two higher valence bands. The positive (negative) logarithmic magnetoconductivity is the signature of the weak localization (antilocalization). (b) No intervalley scattering ($\tau_0/\tau_1 = 0$) for different V . (c) At $V = 0.1$ eV and for different τ_0/τ_1 , the ratio between intervalley and intravalley scattering rates. (d) Zoom-in of (c) for $\tau_0/\tau_1 = 0.1, 1, 10$. Parameters: $\Delta = 1.66$ eV and $\lambda = 0.075$ eV [15], mean free path $\ell = 10$ nm, and phase coherence length $\ell_\phi = 300$ nm.

symmetry because of the opposite spin splitting at the two valleys (Fig. 1). For two possible spin-flip mechanisms, the magnetic scattering and spin-orbit scattering, the latter is likely to exist in the materials. The spin-orbit scattering preserves time-reversal symmetry, along with the broken spin-rotational symmetry, it has the symplectic symmetry [24] which leads to WAL [25].

To test the above picture, we calculated the WL and WAL using the diagrammatic techniques [26–30]. Because the results for gapless graphene without spin-orbit coupling can not be applied directly, we generalize the calculation to this multi-valley massive Dirac cones coupled by intervalley spin-orbit scattering. The method is based on the perturbation expansion of the Kubo formula for conductivity. The Hamiltonian in Eq. (1) is taken as the unperturbed part and scattering potentials as perturbations. The scattering potentials are given as follows. The spin-conserved intravalley scattering is modeled by

$$U_{\mathbf{k},\mathbf{k}'}^0 = \sum_{\mathbf{R}} u_{\mathbf{R}} e^{i(\mathbf{k}'-\mathbf{k})\cdot\mathbf{R}}, \quad (3)$$

where $u^{\mathbf{R}}$ is the potential of an impurity at position \mathbf{R} . The subscript \mathbf{k}, \mathbf{k}' means the potential scatters an electron of wavevector \mathbf{k}' to \mathbf{k} . The spin-flip intervalley scattering is given by spin-orbit scattering

$$U_{\mathbf{k}, \mathbf{k}'}^{\text{I,so}} = \begin{bmatrix} U_z^A & 0 & U_-^A & 0 \\ 0 & U_z^B & 0 & U_-^B \\ U_+^A & 0 & -U_z^A & 0 \\ 0 & U_+^B & 0 & -U_z^B \end{bmatrix},$$

$$U_z^{A/B} = i \sum_{\mathbf{R} \in A/B} u^{\mathbf{R}} e^{i(\mathbf{k}' - \mathbf{k}) \cdot \mathbf{R}} \mathbf{k} \times \mathbf{k}' \cdot \hat{z},$$

$$U_{\pm}^{A/B} = i \sum_{\mathbf{R} \in A/B} u^{\mathbf{R}} e^{i(\mathbf{k}' - \mathbf{k}) \cdot \mathbf{R}} \mathbf{k} \times \mathbf{k}' \cdot (\hat{x} \pm i\hat{y}), \quad (4)$$

where the matrix is spanned by the basis functions in the order of $|\uparrow A\rangle, |\uparrow B\rangle, |\downarrow A\rangle, |\downarrow B\rangle$, and $\hat{x}, \hat{y}, \hat{z}$ stand for the unit vectors. The extra i in $U_{\mathbf{k}, \mathbf{k}'}^{\text{I,so}}$ protects time-reversal symmetry in spin-orbit scattering as $i, \mathbf{k}, \mathbf{k}'$, and spin change sign under time reversal. For mathematical simplicity, we assumed short-range and delta correlation for both U^0 and $U^{\text{I,so}}$. Although intravalley scattering should be related to long-range potential, the practice by the delta potential was justified [31].

From the diagrammatic techniques, the total conductivity is given by

$$\sigma = \sigma^D + \sigma^F, \quad (5)$$

where σ^D is the semiclassical (Drude) conductivity. According to the Einstein relation, σ^D is given by

$$\sigma^D = e^2 N_F D \quad (6)$$

where $N_F = E_F / (\pi \hbar^2 v^2)$ is the density of states at the Fermi surface with E_F the Fermi energy measured from the Dirac point, $D = \eta_v v_F^2 \tau / 2$ is the diffusion constant with η_v the ladder diagram correction to the velocity of Dirac fermions [32], v_F the Fermi velocity, and the total scattering time given by $\tau = (1/\tau_0 + 1/\tau_1)^{-1}$, where τ_0 and τ_1 are intravalley and intervalley scattering times, respectively. Therefore, σ^D is a function of the total scattering time, thus can not distinguish the contributions from intervalley and intravalley scattering. Besides, σ^D is insensitive to magnetic field. For these reasons, the quantum interference correction to the Drude conductivity σ^F (quantum conductivity for short) has to be considered, which is found to take the form of logarithmic functions

$$\sigma^F = \frac{e^2}{\pi \hbar} \left(C_0 \ln \frac{X_0^{-2} + \ell_\phi^{-2}}{X_0^{-2} + \ell^{-2}} + C_1 \ln \frac{X_1^{-2} + \ell_\phi^{-2}}{X_1^{-2} + \ell^{-2}} \right), \quad (7)$$

where C_1 and C_0 are weight factors for the intravalley and intervalley contributions. X_0 and X_1 are corresponding characteristic lengths that effectively reduce the mean free path ℓ and phase coherence length ℓ_ϕ . The intervalley/intravalley scattering ratio is incorporated in the

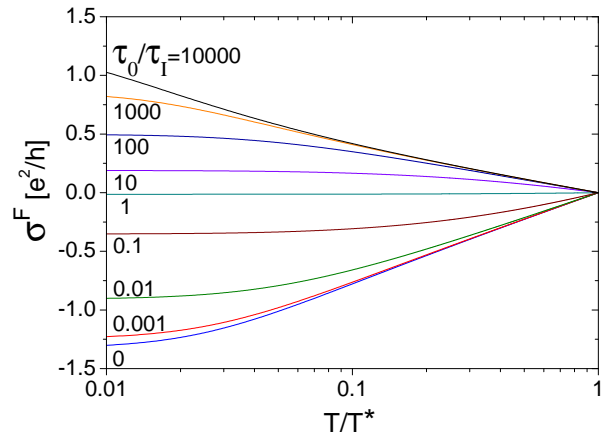


FIG. 3: Zero-field quantum conductivity σ^F as a function of temperature T for different τ_0/τ_1 . Positive (negative) σ^F corresponds to weak antilocalization (localization). Other parameters are the same as those in Figs. 2 (c) and (d).

analytic expressions for $C_{0,I}$ and $X_{0,I}$ [33]. Due to its quantum interference origin, σ^F can be suppressed by a perpendicular magnetic field B_z , leading to a magnetoconductivity

$$\Delta\sigma(B_z) \equiv \sigma^F(B_z) - \sigma^F(0) = \frac{e^2}{\pi \hbar} (C_0 F_0 + C_1 F_1), \quad (8)$$

where $F_i = \Psi(\ell_B^2/\ell_i^2 + \frac{1}{2}) - \ln(\ell_B^2/\ell_i^2)$, $1/\ell_i^2 \equiv 1/\ell_\phi^2 + 1/X_i^2$, Ψ is the digamma function, and $\ell_B \equiv \sqrt{\hbar/(4e|B_z|)}$ is the magnetic length [33].

Figure 2(b) shows the magnetoconductivity in the absence of intervalley scattering, and when the Fermi energy intersects with the two highest valence bands. The WL is a quantum interference induced suppression of conductivity, which can be lifted by magnetic field and gives positive magnetoconductivity. Figure 2(b) shows that the magnetoconductivity is always positive in the allowed range of the Fermi energy, indicating the WL from each valence band. Figures 2(c) and (d) shows the magnetoconductivity as the intervalley scattering increases. It is convenient to define the ratio between intervalley spin-orbit and intravalley scattering rates

$$\tau_0/\tau_1, \quad (9)$$

which increases with increasing intervalley scattering. In Figs. 2(c) and (d), as τ_0/τ_1 increases, the magnetoconductivity changes from positive to negative, corresponding to a crossover from WL to WAL. The magnetoconductivity covers a wide range of τ_0/τ_1 , from < 0.001 to > 1000 . When $\tau_0/\tau_1 > 10$ or < 0.1 , the magnetoconductivity changes sensitively with τ_0/τ_1 . This sensitivity allows us to estimate even a very small τ_1 when τ_0 dominates, or vice versa. Considering the low mobility in

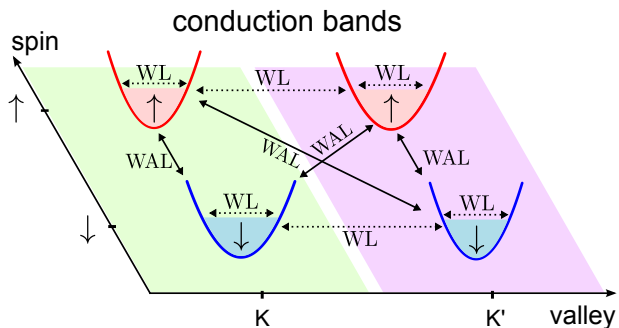


FIG. 4: Weak localization (WL) and antilocalization (WAL) in the conduction bands. Spin-up (↑) and spin-down (↓) are offset for clarity. Solid and dotted arrows represent spin-orbit and spin-conserved scattering, respectively.

MX_2 [20], the calculation has assumed a short total scattering time τ as well as short mean free path $\ell \equiv \sqrt{D\tau}$, then the results are not sensitive to ℓ and τ , which are fixed throughout the paper. Note that similar crossover also happened in graphene but is completely opposite [26, 34] because graphene is gapless and has ignorable spin-orbit interaction [35, 36].

The temperature dependence of the quantum conductivity σ^F also provides the signature of the crossover. Because the weak (anti-)localization comes from the quantum interference, their temperature dependence mainly originates from the phase coherence length ℓ_ϕ . In the quantum diffusion regime, ℓ_ϕ becomes much longer than the mean free path ℓ and increases with decreasing temperature as decoherence mechanisms from electron-phonon and electron-electron interactions are suppressed. The similarity of band dispersion to the conventional two-dimensional systems [37] allows us to assume that $\ell_\phi = C_{ph}(T/T^*)^{-3/2} + C_{ee}(T/T^*)^{-1/2}$, where the coefficients C_{ph} from electron-phonon and C_{ee} from electron-electron interactions are determined by imposing that $\ell_\phi = 300$ nm at $T/T^* = 0.01$ and $\ell_\phi = \ell$ at $T/T^* = 1$. T^* is a characteristic temperature above which the system transits from the quantum to classical diffusion regimes, so σ^F vanishes at $T = T^*$. The order of magnitude for T^* ranges between 10 and 100 K [37–39]. Figure 3 shows $\sigma^F(T)$ in Eq. (7) for different τ_0/τ_1 . The crossover from WL to WAL can be read from the sign of σ^F turning from negative to positive. Note that the total conductivity is $\sigma(T) = \sigma^D(T) + \sigma^F(T, B)$, where the Drude conductivity σ^D may give extra temperature power law that depends on scattering mechanisms [38, 39]. But σ^F from the weak (anti-)localization is the contribution most sensitive to magnetic field (because of the logarithmic dependence). σ^F thus can be extracted from the total conductivity by $\sigma^F(T) = \sigma(T, B_c) - \sigma(T, 0)$, with B_c a finite magnetic field large enough to quench the weak (anti-)localization, say, of 1 Tesla.

We can also have some qualitative arguments for the

conduction bands. All four conduction bands can take part in transport as they always intersect the Fermi surface together. Therefore, different from the transport in hole-doped samples, both intravalley spin-orbit and intervalley spin-conserved scattering are possible in the conduction bands. The rule is that spin-flip scattering assisted by spin-orbit interaction leads to WAL while spin-conserved scattering to WL because the pseudo-spin degrees of freedom is frozen. All types of scattering and the resulting weak (anti-)localization are shown in Fig. 4.

This work was supported by the Research Grant Council of Hong Kong under Grant No. HKU 705110P (H.Z.L. and S.Q.S.) and HKU 706412P (W.Y.). D.X. was supported by the U.S. Department of Energy, Office of Basic Energy Sciences, Materials Sciences and Engineering Division.

-
- [1] O. Gunawan, Y. P. Shkolnikov, K. Vakili, T. Gokmen, E. P. De Poortere, and M. Shayegan, *Phys. Rev. Lett.* **97**, 186404 (2006).
 - [2] A. Rycerz, J. Tworzydło, and C. W. J. Beenakker, *Nature Phys.* **3**, 172 (2007).
 - [3] D. Xiao, W. Yao, and Q. Niu, *Phys. Rev. Lett.* **99**, 236809 (2007).
 - [4] W. Yao, D. Xiao, and Q. Niu, *Phys. Rev. B* **77**, 235406 (2008).
 - [5] W. Yao, S. A. Yang, and Q. Niu, *Phys. Rev. Lett.* **102**, 096801 (2009).
 - [6] C. C. Liu, W. Feng, and Y. Yao, *Phys. Rev. Lett.* **107**, 076802 (2011).
 - [7] B. Lalmi, H. Oughaddou, H. Enriquez, A. Kara, S. Vizzini, B. Ealet, and B. Aufray, *Appl. Phys. Lett.* **97**, 223109 (2010).
 - [8] P. De Padova, C. Quaresima, C. Ottaviani, P. M. Sheverdyaeva, P. Moras, C. Carbone, D. Topwal, B. Olivieri, A. Kara, H. Oughaddou, B. Aufray, and G. Le Lay, *Appl. Phys. Lett.* **96**, 261905 (2010).
 - [9] B. Aufray, A. Kara, S. Vizzini, H. Oughaddou, C. Lzandri, B. Ealet, and G. Le Lay, *Appl. Phys. Lett.* **96**, 183102 (2010).
 - [10] L. Chen, C. C. Liu, B. Feng, X. He, P. Cheng, Z. Ding, S. Meng, Y. Yao, and K. Wu, *Phys. Rev. Lett.* **109**, 056804 (2012).
 - [11] K. S. Novoselov, D. Jiang, F. Schedin, T. J. Booth, V. V. Khotkevich, S. V. Morozov, and A. K. Geim, *Proc. Natl. Acad. Sci. U.S.A.* **102**, 10 451 (2005).
 - [12] K. F. Mak, C. Lee, J. Hone, J. Shan, and T. F. Heinz, *Phys. Rev. Lett.* **105**, 136805 (2010).
 - [13] A. Splendiani, L. Sun, Y. Zhang, T. Li, J. Kim, C.-Y. Chim, G. Galli, and F. Wang, *Nano Lett.* **10**, 1271 (2010).
 - [14] S. Lebègue and O. Eriksson, *Phys. Rev. B* **79**, 115409 (2009).
 - [15] D. Xiao, G. B. Liu, W. X. Feng, X. D. Xu, and W. Yao, *Phys. Rev. Lett.* **108**, 196802 (2012).
 - [16] H. L. Zeng, J. F. Dai, W. Yao, D. Xiao, and X. D. Cui, *Nature Nanotech.* **7**, 490 (2012).
 - [17] K. F. Mak, K. He, J. Shan, and T. F. Heinz, *Nature*

- Nanotech. **7**, 494 (2012).
- [18] T. Cao, G. Wang, W. Han, H. Ye, C. Zhu, J. Shi, Q. Niu, P. Tan, E. Wang, B. Liu, and J. Feng. Nature Comms, **3**, 887 (2012).
- [19] V. Podzorov, M. E. Gershenson, Ch. Kloc, R. Zeis, and E. Bucher, Appl. Phys. Lett. **84**, 3301 (2004).
- [20] B. Radisavljevic, A. Radenovic, J. Brivio, V. Giacometti, and A. Kis, Nature Nanotech. **6**, 147 (2011).
- [21] H. Fang, S. Chuang, T. C. Chang, K. Takei, T. Takahashi, and A. Javey, Nano Lett. **12**, 3788 (2012).
- [22] Z. Y. Zhu, Y. C. Cheng, and U. Schwingenschlögl, Phys. Rev. B **84**, 153402 (2011).
- [23] D. Xiao, M. C. Chang, and Q. Niu, Rev. Mod. Phys. **82**, 19592007 (2010).
- [24] F. J. Dyson, J. Math. Phys. **3**, 140 (1962).
- [25] S. Hikami, A. Larkin, and Y. Nagaoka, Prog. Theor. Phys. **63**, 707 (1980).
- [26] H. Suzuura and T. Ando, Phys. Rev. Lett. **89**, 266603 (2002).
- [27] E. McCann, *et al.*, Phys. Rev. Lett. **97**, 146805 (2006).
- [28] G. Bergmann, Phys. Rep. **107**, 1 (1984).
- [29] K. I. Imura, Y. Kuramoto, and K. Nomura, Phys. Rev. B **80**, 085119 (2009).
- [30] H. Z. Lu, J. R. Shi, and S. Q. Shen, Phys. Rev. Lett. **107**, 076801 (2011).
- [31] X. Z. Yan and C. S. Ting, Phys. Rev. Lett. **101**, 126801 (2008).
- [32] N. H. Shon and T. Ando, J. Phys. Soc. Jpn. **67**, 2421 (1998).
- [33] Supplementary material.
- [34] F.V. Tikhonenko, A. A. Kozikov, A. K. Savchenko, and R.V. Gorbachev, Phys. Rev. Lett. **103**, 226801 (2009).
- [35] H. Min, J. E. Hill, N. A. Sinitsyn, B. R. Sahu, L. Kleinman, and A. H. MacDonald, Phys. Rev. B **74**, 165310 (2006).
- [36] Y. Yao, F. Ye, X.-L. Qi, S.-C. Zhang, and Z. Fang, Phys. Rev. B **75**, 041401 (2007).
- [37] P. A. Lee and T. V. Ramakrishnan, Rev. Mod. Phys. **57**, 287 (1985).
- [38] T. Ando, A. B. Fowler, and F. Stern, Rev. Mod. Phys. **54**, 437 (1982).
- [39] S. Das Sarma, S. Adam, E. H. Hwang, and E. Rossi, Rev. Mod. Phys. **83**, 407 (2011).